Duty cycle of the radio galaxy B2 0258+35

M. Brienza[1,2], R. Morganti[1,2], M. Murgia[3], N. Vilchez[4], B. Adebahr[1], E. Carretti[3,7], R. Concu[3], F. Govoni[3],
J. Harwood[1], H. Intema[5], F. Loi[3,6], A. Melis[3], R. Paladino[7], S. Poppi[3], A. Shulevski[1], V. Vacca[3], and G. Valente[8]

[1] ASTRON, The Netherlands Institute for Radio Astronomy, Postbus 2, 7990 AA Dwingeloo, The Netherlands
  e-mail: m.brienza@ira.inaf.it
[2] Kapteyn Astronomical Institute, Rijksuniversiteit Groningen, Landleven 12, 9747 AD Groningen, The Netherlands
[3] INAF – Osservatorio Astronomico di Cagliari, Via della Scienza 5, 09047 Selargius (CA), Italy
[4] Qatar Environment and Energy Research Institute (QEERI), HBKU, Qatar Foundation, PO Box 5825, Doha, Qatar
[5] Leiden Observatory, Leiden University, Niels Bohrweg 2, 2333 CA Leiden, The Netherlands
[6] Dipartimento di Fisica, University of Cagliari, Strada Prov.le Monserrato-Sestu Km 0.700, 09042 Monserrato (CA), Italy
[7] INAF – Istituto di Radioastronomia, Via Piero Gobetti 101, 40129 Bologna, Italy
[8] Agenzia Spaziale Italiana (ASI), Roma, Italy

Received 17 February 2018 / Accepted 16 July 2018

ABSTRACT

Context. Radio loud active galactic nuclei (AGN) are episodic in nature, cycling through periods of activity and quiescence. The study of this duty cycle has recently gained new relevance because of the importance of AGN feedback for galaxy evolution.
Aims. In this work we investigate the duty cycle of the radio galaxy B2 0258+35, which was previously suggested to be a restarted radio galaxy based on its morphology. The radio source consists of a pair of kpc-scale jets embedded in two large-scale lobes ($\sim$240 kpc) with relaxed shape and very low surface brightness, which resemble remnants of a past AGN activity.
Methods. We have combined new LOFAR data at 145 MHz and new Sardinia Radio Telescope data at 6600 MHz with available WSRT data at 1400 MHz to investigate the spectral properties of the outer lobes and derive their age.
Results. Interestingly, the spectrum of both the outer northern and southern lobes is not ultra-steep as expected for an old ageing plasma with spectral index values equal to $\alpha_{1400}^{145} = 0.48 \pm 0.11$ and $\alpha_{6600}^{1400} = 0.69 \pm 0.20$ in the outer northern lobe, and $\alpha_{1400}^{145} = 0.73 \pm 0.07$ in the outer southern lobe. Moreover, despite the wide frequency coverage available for the outer northern lobe (145–6600 MHz), we do not identify a significant spectral curvature (SPC $\simeq 0.2 \pm 0.2$).
Conclusions. While mechanisms such as in-situ particle reacceleration, mixing or compression can temporarily play a role in preventing the spectrum from steepening, in no case seem the outer lobes to be compatible with being very old remnants of past activity as previously suggested (with age $\gtrsim$80 Myr). We conclude that either the large-scale lobes are still fuelled by the nuclear engine or the jets have switched off no more than a few tens of Myr ago, allowing us to observe both the inner and outer structure simultaneously. Our study shows the importance of combining morphological and spectral properties to reliably classify the evolutionary stage of low surface brightness, diffuse emission that low frequency observations are revealing around a growing number of radio sources.

Key words. radio continuum: galaxies – galaxies: jets – galaxies: individual: NGC 1167 – galaxies: individual: B2 0258+35

1. Introduction

Some of the outstanding questions in the study of radio-loud active galactic nuclei (AGN) are concerned with how long and how frequently they are active, and how to identify the various phases of their evolution. Statistical studies and models suggest that the AGN duty cycle strongly depends on the power of the radio source (Best et al. 2005; Shabala et al. 2008; Turner & Shabala 2015) but precise estimates are still not available. Understanding the life cycle of AGN jets has recently gained a new broader relevance in the context of radio galaxy evolution (Morganti 2017), as they can transfer a significant amount of energy into the ambient medium (McNamara & Nulsen 2007; Wagner & Bicknell 2011; Wagner et al. 2012; Gaspari et al. 2012). Feedback from AGN is indeed required by all cosmological simulations to explain the quenching of the star formation in early type galaxies and the correlation between galaxy, and black hole properties (Di Matteo et al. 2005; Fabian 2012; Schaye et al. 2015; Sijacki et al. 2015).

Radio observations are particularly suited to trace the different stages of evolution in radio galaxies via the study of their radio morphology and spectra. Evidence of radio galaxies in different phases of their evolution has been presented in the literature as described below.

For example, remnant radio galaxies represent the last phase when the jets have switched off (e.g. Parma et al. 2007; Murgia et al. 2011; Saripalli et al. 2012). Recent studies based on low frequency observations and modelling of radio galaxies find fractions of remnants $\lesssim$10–15%, suggesting a rapid expansion of the plasma in the ambient medium after the nuclear activity has ceased (Godfrey et al. 2017; Brienza et al. 2017; Mahatma et al. 2018). Observations show that remnants can have different characteristics, probably depending on their stage of evolution. At GHz frequencies they are commonly observed to have ultra-steep spectra (S $\propto \nu^{-\alpha}$, $\alpha > 1.2$, e.g. Parma et al. 2007; Hurley-Walker et al. 2015; Shulevski et al. 2017), typical of old ageing plasma, but can also have only moderately steep spectra at MHz frequencies ($0.6 < \alpha < 1$, e.g. Murgia et al. 2011; Brienza et al. 2016; Mahatma et al. 2018). Moreover, they

can show very weak radio cores indicating that the nuclear activity may not completely switch off but just go through a period of significant suppression (Murgia et al. 2011; Brienza et al. 2016, 2017; Mahatma et al. 2018).

Sources that exhibit remnant emitting plasma from past activity and, at the same time, new-born jets are named restarted radio galaxies (see Saikia & Jamrozy 2009, for a review). These can be effectively used to investigate the duty cycle of the radio AGN.

The most explicit and well-known signatures of recurrent jet activity on large scales are "double-double radio galaxies" (DDRGs). This class of objects was first defined by Schoenmakers et al. (2000) as "radio galaxies consisting of a pair of double radio sources with a common centre" and further investigated by other authors (e.g. Kaiser et al. 2000; Konar & Hardcastle 2013; Orrù et al. 2015). For these objects the duration of the quiescent phase between two episodes of jet activity is estimated to be in the range $10^5 - 10^7$ yr, and is found to be typically shorter than the duration of the previous active phase equal to 10^8 yr on average (Konar et al. 2013). However, the phenomenon of restarted AGN is not limited to DDRGs. Another class of sources is observed to have compact inner jets embedded in large-scale, low-surface brightness lobes (e.g. Jamrozy et al. 2009; Kuźmicz et al. 2017). In some of these sources, there are indications that the quiescent phase may be as long as $\geq 10^8$ yr (Jamrozy et al. 2007). Among the most famous cases of restarted jets is the radio galaxy Centaurus A, where more than one phase of activity has been claimed based on the presence of two distinct morphology structures (Morganti et al. 1999; McKinley et al. 2013, 2018). Moreover, observations of remnant emission on small scales (<100 pc) associated to active compact radio galaxies (Luo et al. 2007; Orienti & Dallacasa 2008) suggest that at the beginning of the jet activity, multiple cycles of short bursts ($10^3 - 10^4$ yr) may occur before the jets start to expand to large scales.

The physical mechanisms that drive the radio jets intermittence are still poorly understood and are possibly related to the galaxy environment. Some possible explanations include gas-rich galaxy-galaxy interactions (e.g. Schoenmakers et al. 2000), perturbations of the accretion process (e.g. Pringle 1997; Czerny et al. 2009; Wu 2009) and chaotic cold accretion (e.g. Gaspari et al. 2013, 2017). Alternative interpretations to the restarting scenario have also been proposed to explain the observed morphologies of these sources. For example, Baum et al. (1990) suggest that compact radio sources can arise within a large-scale radio galaxy if the jet propagation is obstructed or impeded on scales of tens of parsecs to few kiloparsecs. In that case, the extended structure would remain visible along with the confined parsec scale source.

The variety of sources described above suggests that a multitude of situations and evolution histories can occur. As a consequence, the interpretation and classification of restarted sources is not trivial and more examples need to be studied in detail for improving our understanding. In particular, extra constraints can be obtained by studying the spectral properties of these sources on a broad spectral range, from MHz to GHz frequencies, in combination with the source morphology. A better characterization of known restarted radio galaxies is also essential for a better selection and census of restarted sources in upcoming large-area radio surveys (e.g. the LOw Frequency ARray (LOFAR) Two-metre Sky Survey – LoTSS, Shimwell et al. 2017).

In this paper we present new observations of the radio source B2 0258+35, where two low-surface brightness extended lobes (240 kpc) have been discovered at 1400 MHz (Shulevski et al.

2012) around a compact radio galaxy (3 kpc). Due to its morphology, this source has been interpreted as a restarted radio galaxy in which the outer lobes represent old remnants of a past AGN activity. The aim of this work is to put new constraints on the physical properties and duty cycle of these lobes by studying their spectral properties and morphology over a wide frequency range.

The cosmology adopted in this work assumes a flat universe and the following parameters: $H_0 = 70 \, \mathrm{km \, s^{-1} \, Mpc^{-1}}$, $\Omega_\lambda = 0.7, \Omega_M = 0.3$. At the redshift of B2 0258+35 equal to $z = 0.0165$ (Wegner et al. 1993), 1 arcsec corresponds to 0.34 kpc. Throughout the paper the spectral index, α, is defined using the convention $S \propto \nu^\alpha$.

2. Overview on the source B2 0258+35

The radio source B2 0258+35 is hosted by the giant early-type galaxy NGC 1167 ($M_B = -21.7$ mag, $D_{25} = 56$ kpc), which is optically classified as a Seyfert 2 galaxy (Ho et al. 1997). The galaxy is located at redshift $z = 0.0165$ (Wegner et al. 1993) and does not belong to any galaxy group but is surrounded by a few smaller satellites (Struve et al. 2010). Deep optical observations show a faint, tightly wound spiral structure at $r < 30$ kpc, which represents the signature of a past major merger event (Emonts et al. 2010).

Indications of past and/or ongoing interactions are also confirmed by the presence and kinematics of a large (~ 160 kpc) and massive HI disk ($M_{HI} = 1.5 \times 10^{10} \, M_\odot$, Noordermeer et al. 2005, Emonts et al. 2010, Struve et al. 2010). This HI structure is thought to have assembled via accretion of gas-rich satellite galaxies. However, the gas distribution is extremely regular out to 65 kpc, with disturbed kinematics only in the very outer part, which is possibly the result of recent interactions with its satellites. Thanks to its inner regular kinematics, Struve et al. (2010) have computed a tight lower limit on the epoch of the last major merger event equal to ~ 1 Gyr. This timescale is also supported by the absence of young stellar population signatures in the optical spectrum (Emonts 2006). However, more recent interactions with small companion galaxies cannot be ruled out.

HI is also observed in absorption against the the central radio source (Emonts et al. 2010; Murthy et al., in prep.). The broad absorption profile is likely the result of the combination of a circumnuclear disk disturbed by the interaction with the radio jet (Murthy et al., in prep.). Support for an on-going interaction also comes from the molecular gas (Murthy et al., in prep. using observations from Prandoni et al. 2007). Surprisingly, there is no evidence of broadening in the optical emission lines of the ionized gas (Emonts 2006; Santoro, priv. comm.).

The central radio source has a luminosity at 408 MHz of $L_{408} = 10^{24.37} \, \mathrm{W \, Hz^{-1}}$ and has been classified as a Compact Steep Spectrum (CSS) source by Sanghera et al. (1995). As shown in the inset in Fig. 1, sub-arsecond imaging shows two plum-like lobes of ~ 3 kpc total projectd size, with jet-like structures but without clear hot-spots (Giroletti et al. 2005; Giovannini et al. 2001). From the jet to counter-jet ratio at 22 000 MHz, Giroletti et al. (2005) have constrained the jets inclination angle to a value in the range 40 deg $< \theta <$ 50 deg, which is in accordance with the optical classification of the parent galaxy. Using radiative evolution models they have derived a source age of 0.9 Myr and, based on dynamical arguments, have suggest that the radio source might not grow into an extended FRI/II radio galaxy. This is further supported by the clear bending of the southern lobe indicating a dense surrounding interstellar medium (ISM), which may be the cause of the source
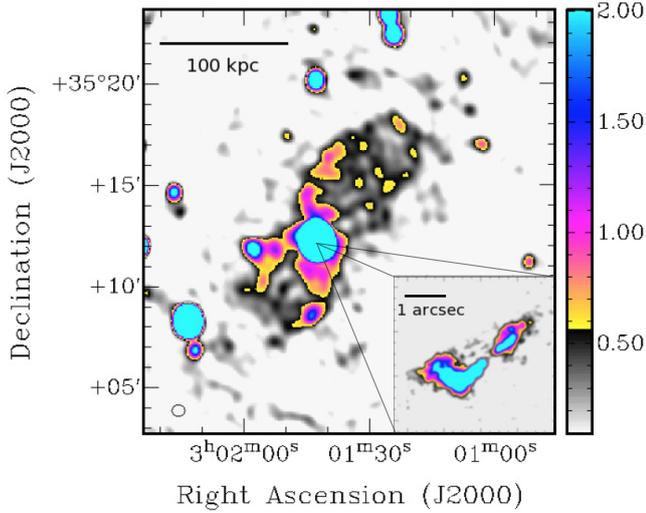
Fig. 1. Continuum image of the radio galaxy B2 0258+35 at 1400 MHz obtained with the Westerbork Synthesis Radio Telescope from Shulevski et al. (2012). The synthesized beam is indicated with the ellipse at bottom left. The intensity ranges from $100\,\mu$Jy (1σ) to 2 mJy (20σ). The inset at the bottom right shows a high-resolution radio image at 8400 MHz of the central CSS source obtained with the Very Large Array by Giroletti et al. (2005).

Table 1. Summary of the properties of the radio source B2 0258+35 and of its host galaxy.

Host galaxy	NGC 1167
M_B	–21.7 mag
D_{25}	56 kpc
Optical classification	Seyfert 2
Redshift	0.0165
Size inner radio lobes	3 kpc
Inner lobes radio power	$L_{408} = 10^{24.37}$ W Hz^{-1}
Size outer radio lobes	240 kpc
M_{HI}	$1.5 \times 10^{10}\,M_\odot$
Diameter Hi disk	160 kpc

Unfortunately, due to the data quality and dynamic range limitations caused by the bright central source, we could not recover the outer lobe emission at 235, 350 and 612 MHz. However, these frequencies have been useful for the study of the compact source. For the analysis of the outer lobes we have also used the WSRT image at 1400 MHz presented by Shulevski et al. (2012). In the following sections we describe the observations and the data reduction procedures. A summary of the observational details is presented in Table 2 and a summary of the final image properties is presented in Table 3.

3.1. LOFAR HBA observations and data reduction

Dedicated observations of the source were performed using the LOFAR High Band Antenna (HBA) on September 13th, 2015. All the 64 antennas of the Dutch Array have been used, providing a maximum baseline of ~100 km. The target was observed in scans of 30 min for a total integration time of 8 h, interleaved by 2-min observations of the flux-density calibrator 3C48. The sampling time was set to 1 s and four polarization products (XX, YY, XY, and YX) were recorded. The total observed bandwidth is equal to 95.1 MHz in the range 100.2–195.3 MHz. This was divided in 487 sub-bands of 195.3 kHz composed of 64 channels each. The observational details are summarized in Table 2.

Using the observatory pipeline (Heald et al. 2010) the data were pre-processed. Data below 108.9 MHz and above 176.9 MHz were flagged and excluded from further processing due to the presence of strong RFIs.

After pre-processing the data were calibrated using the classical direction-indipendent procedure (e.g. Brienza et al. 2016; Mahony et al. 2016). Amplitude and phase solutions for each station were calculated according to the model of 3C48 presented by Scaife & Heald (2012) and transferred to the target field. The data were then combined into groups of ten sub-bands (corresponding to a bandwidth of ~2 MHz) and phase self-calibrated iteratively, adding progressively longer baselines. The LOFAR imager AWImager (Tasse et al. 2013) was used for the imaging, which performs both w-projection to account for non-coplanar effects (Cornwell & Perley 1992) and A-projection to account for the changing beam throughout the observation (Bhatnagar et al. 2008).

We produced images at different resolutions and with different weightings. The best detection of the outer lobes was achieved with a uv-cut equal to 2 kλ, robust weighting equal to 0 and final resolution of 80 arcsec × 98 arcsec. Hints of the lobes emission are observed at higher resolution too but the image quality is not enough for a reliable detection and flux density measurement of the low surface brightness

confinement and is in agreement with the jet-ISM interaction inferred from HI absorption (Murthy et al., in prep.). The spectral index distribution within the CSS source varies from $\alpha_{8.4}^{22} = 0$ in the core, to $\alpha_{8.4}^{22} = 0.6$ in the jet-like structures within the lobes, to $\alpha_{8.4}^{22} = 1.0 - 1.5$ in the surrounding diffuse emission (Giroletti et al. 2005).

A very interesting ingredient for understanding the evolutionary history of the source is the presence of two large-scale (240 kpc), low-surface brightness (1.4 mJy arcmin^{-2} at 1400 MHz) lobes that surround the CSS source. These have been first detected and studied at 1400 MHz by Shulevski et al. (2012) using the Westerbork Synthesis Radio Telescope (WSRT; Fig. 1). The authors propose that the lobes represent old remnants of a previous cycle of jet activity. The S-shape morphology of the broad enhancements in surface brightness located at the edges of the outer lobes is also notable.

Assuming the lobes to be buoyant bubbles expanding in the intergalactic medium, Shulevski et al. (2012) estimate the dynamical age of the source to be $\gtrsim 80$ Myr. Because the age of the young central CSS source is about 0.9 Myr, they suggest that the quiescent phase between the two radio bursts has lasted ~100 Myr.

The main characteristics of the radio source B2 0258+35 and of its host galaxy are summarised in Table 1.

3. Data

To investigate the radio spectral properties of the extended lobes and to constrain any spectral curvature, we expand here the study at 1400 MHz presented by Shulevski et al. (2012) to other frequencies. We have performed observations at 145, 350 and 6600 MHz using the Low-frequency Array (LOFAR, van Haarlem et al. 2013), the Karl G. Jansky Very Large Array (VLA), and the Sardinia Radio Telescope (SRT, Bolli et al. 2015; Prandoni et al. 2017) respectively. Moreover, we have reprocessed archival observations of the Giant Metrewave Radio Telescope (GMRT; Swarup 1991) taken at 235 and 612 MHz.

Table 2. Summary of the observational details.

Telescope	Configuration	Frequencies MHz	Target TOS (h)	Calibrator	Calibrator TOS (h)	Observation date
LOFAR	HBA Inner	118.9–176.9	8	3C48	0.53	13 September 2015
GMRT[a]	–	235	2.3	3C48, 0432+416	0.75	24–25 July 2011
VLA	CnB-B	224–480	2.25	3C48	0.5	6 February–10 April 2015
GMRT[a]	–	612	2.3	3C48, 0432+416	0.75	24–25 July 2011
SRT	–	6000–7200	11	3C286, 3C138	2	1-2-6-7 February 2016

Notes. [a] Archival observations.

Table 3. Summary of the image properties at different frequencies.

| Frequency MHz	$FWHM$ arcsec^2	RMS mJy beam^{-1}
145	80×98	3
235	9.3×13.6	1.2
350	30×30	1.2
612	3.6×6.5	0.2
1400[a]	33×39	0.1
6600	174×174	0.9

Notes. [a] Image taken from Shulevski et al. (2012).

emission due to the presence of deconvolution artefacts associated with the strong central source. The calibration scheme created by van Weeren et al. (2016) and Williams et al. (2016), which corrects for direction-dependent errors due to ionospheric phase and amplitude distortions, did not provide any significant improvement of the dynamic range at resolutions higher than 80 arcsec × 98 arcsec.

Therefore, in the following work we have used the image obtained with the original direction-independent calibrated data. The final image was obtained by combining all images at different frequencies in the image plane. It has a central frequency of 145 MHz, a spatial resolution of 80 arcsec × 98 arcsec and a noise of 3 mJy beam^{-1} in the proximity of the target (see Fig. 2, top panel).

3.2. SRT observations and data reduction

The source was observed with the SRT on February 1-2-6-7, 2016 as part of the early science programme "SRT Multifrequency Observations of Galaxy Clusters" (SMOG – PI M. Murgia, see also Govoni et al. 2017; Loi et al. 2017; Vacca et al. 2018). A region of 0.7 deg × 0.7 deg was mapped using the C-Band receiver for a total of 11 h. We performed several on-the-fly (OTF) mappings in the equatorial frame in both right ascension (RA) and declination (Dec). The FWHM of the beam at this frequency is 2.9 arcmin so we set the telescope scanning speed to 6 arcmin s^{-1} and the scan separation to 0.7 arcmin to properly sample the beam. Full Stokes parameters were recorded with the SARDARA backend (SArdinia Roach2-based Digital Architecture for Radio Astronomy; Murgia et al. 2016; Melis et al. 2018). The correlator configuration was set to 1024 frequency channels of approximately 1.46 MHz for a total bandwidth of 1500 MHz. We then set the Local Oscillator to 5900 MHz and we used a filter to select frequency range from 6000 to 7200 MHz, which is relatively free from strong RFIs. The central frequency is thus 6600 MHz and the total bandwidth is 1200 MHz. A summary of the SRT observations is listed in Table 2.
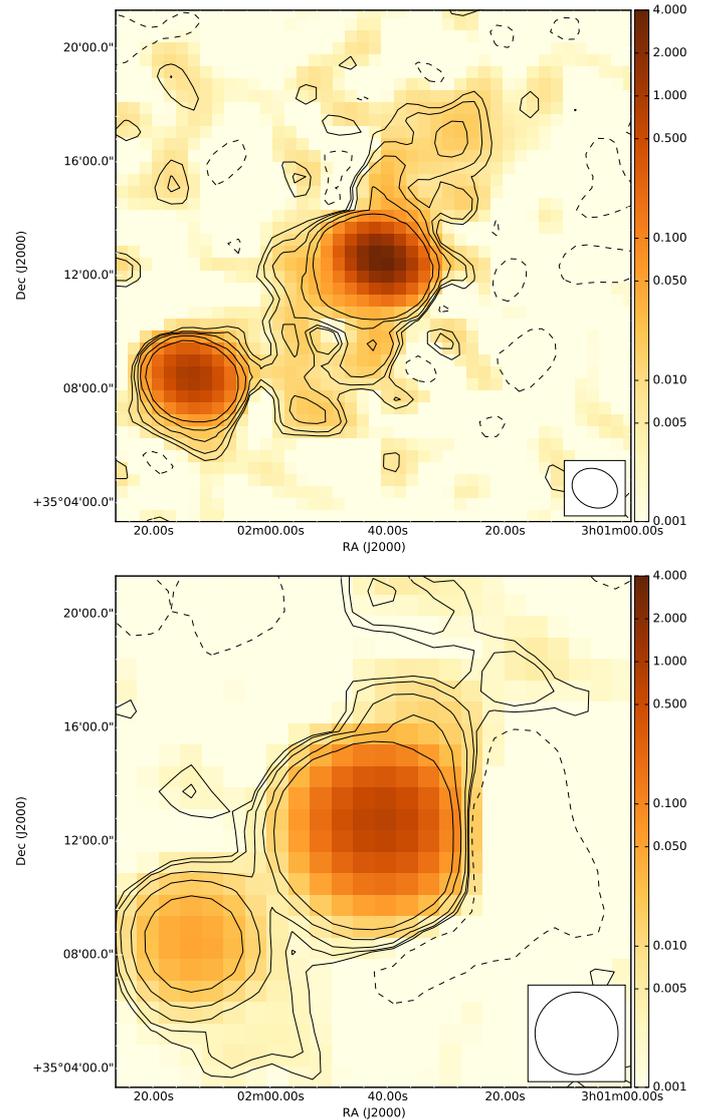
Fig. 2. Radio maps of the source B2 0258+35. *Top panel*: LOFAR 145-MHz map at 80 arcsec × 98 arcsec resolution. Levels: −2, 2, 3, 5, 10, 20 × σ (3 mJy beam^{-1}). *Bottom panel*: SRT 6600-MHz map at 2.9-arcmin resolution. Levels: −2, 2, 3, 5, 10, 20 × σ (0.9 mJy beam^{-1}). The colour scale is set in Jy beam^{-1}. In both panels the beam is shown at the bottom right corner.

After flagging RFIs, we performed the bandpass and flux-density calibration using observations of the sources 3C286 and 3C138. The flux density scale was set according to Perley & Butler (2013). All data observed during February 7th,

were completely discarded due to low quality resulting from bad weather conditions during the observing run. We processed the data using the proprietary Single-dish Spectral-polarimetry Software (SCUBE; Murgia et al. 2016). We applied the gain-elevation curve correction to account for the gain variation with elevation caused by the telescope structure changes due to the gravitational stress.

We proceeded with fitting the baseline with a second order polynomial and subtracting it from each calibrated scan. To perform the imaging we projected the data in a regular three-dimensional grid with a spatial resolution of 42 arcsec pixel^{-1} so that four pixels subtend the beam FWHM. All scans along the two orthogonal axes (RA and Dec) were then stacked together to produce the Stokes I image. In the combination, the individual image cubes were averaged and de-stripped by mixing their Stationary Wavelet Transform (SWT) coefficients as described in Murgia et al. (2016). We then used the higher signal-to-noise image cubes obtained from the SWT stacking as a prior model to refine the baseline fit.

Because the central source is very strong, a high dynamical range was required to be able to detect the extended, low surface brightness lobes in the central region of the map. To achieve this goal we deconvolved the sky image with a beam model pattern following Murgia et al. (2016) in order to remove the beam sidelobes. The deconvolution algorithm interactively finds the peak in the image obtained from the SWT stacking of all images and subtracts a fixed gain fraction (typically 0.1) of this point source flux convolved with the re-projected telescope "dirty beam model" from the individual images. In the re-projection, the exact elevation and parallactic angle for each pixel in the unstacked images are used. The residual images were stacked again and the CLEAN continued until convergence. As a final step, CLEAN components at the same position were merged, smoothed with a circular Gaussian beam with *FWHM* 2.9 arcmin, and then restored back in the residuals image to obtain a CLEANed image. The final image obtained in this way has a noise of 0.9 mJy beam^{-1} and is shown in Fig. 2 (bottom panel).

3.3. VLA P-band observations and data reduction

We performed observations of the source with the VLA in two slots on February 6th, 2015 and April 10th, 2015 with the *P*-band receiver. On both runs, 27 antennas were used, distributed in CnB-B and B configuration in the two different runs respectively. The target and flux density calibrator 3C48 were observed for 1.5 h and 20 min on the first day and 45 min and ten minutes on the second day respectively. The sampling time was set to 2 s and four polarization products (RR, LL, RL, and LR) were recorded. The total bandwidth, equal to 256 MHz in the range 224–480 MHz, was divided by default in 16 sub-bands of 16 MHz with 128 frequency channels. The observational details are summarized in Table 2.

All datasets were reduced using the following steps. After having applied the flags suggested by the observatory, the data were flagged automatically using the AOFlagger, visually checked and further manually flagged when required. We used the Common Astronomy Software Applications (CASA, version 4.7, McMullin et al. 2007) to perform the calibration in the standard manner and following the guidelines set out in the online tutorial for continuum *P*-band data[1]. The flux scale was

---

[1] https://casaguides.nrao.edu/index.php/VLA_Radio_galaxy_3C_129:_P-band_continuum_tutorial-CASA4.7.0

set according to Scaife & Heald (2012). Phase and amplitude self-calibration was performed. The final image of the field is 2 deg × 2 deg in size and was made using a Brigg's weighting with a robustness parameter of 0. The image has a resolution of 30 arcsec × 30 arcsec and central noise of ∼1.2 mJy beam^{-1}. As already mentioned, due to severe flagging caused by the presence of extensive RFIs and the dynamic range limitations caused by the bright central source, the sensitivity of the data is not sufficient to detect the low surface brightness emission of the outer lobes of the radio galaxy.

3.4. GMRT observations and data reduction

We used archival data of the GMRT at 235 and 612 MHz. The observations were performed on July 24th and 25th, 2011. The target was observed in five time-scans for a total integration time of 2.3 h. The source 3C48 was used as flux-density calibrator and observed at the beginning and at the end of the observing run for ten minutes respectively. We adopt the Scaife-Heald model (Scaife & Heald 2012) for setting the absolute flux scale. Data at both frequencies were recorded simultaneously in single-polarization mode using a 33-MHz bandwidth divided into 512 channels of 65-kHz bandwidth and a sampling time of 16.1 s.

We processed the data using the SPAM pipeline (Intema 2014; Intema et al. 2017). The output calibrated visibility data were imported into CASA to produce images at different resolutions. By using uniform weighting during imaging, we obtained a resolution of 3.6 arcsec × 6.5 arcsec and 9.3 arcsec × 13.6 arcsec in the 612-MHz map and 235-MHz maps, respectively. The noise is equal to 200 mJy beam^{-1} at 612 MHz and 1.2 mJy beam^{-1} at 235 MHz. We also imaged the data using Briggs weighting with robust = 0 and uvtaper = 40 arcsec to enhance the large-scale emission. The final images with ∼40 arcsec resolution have a noise levels equal to ∼1.2 mJy beam^{-1} and 12 mJy beam^{-1} at 612 MHz and at 235 MHz, respectively. Unfortunately, with neither imaging weighting schemes we managed to detect the low surface brightness emission of the outer lobes of the radio galaxy.

4. Results

4.1. Morphology

In Fig. 2 we show the two radio continuum images of the source B2 0258+35 where the outer lobes are detected at 145 MHz and 6600 MHz respectively. As already mentioned in Sect. 2, the low surface brightness emission of the outer lobes has not been recovered at either 235 MHz, 350 MHz or 612 MHz, therefore we do not show those images here. We also note the presence of a point-like unrelated source located in south-east direction (RA 03:02:13.12, Dec +35:08:20.79, J2000).

In the LOFAR map both lobes are clearly visible. Their linear extension and morphology is in general agreement with what has been previously observed at 1400 MHz (240 kpc, Shulevski et al. 2012). We measure a total angular extension of ∼13 arcmin, using the 3σ contours at the tip of each lobe as a reference, which corresponds to a linear size equal to ∼265 kpc. The observed size difference with respect to Shulevski et al. (2012) may be partially attributed to the lower resolution of the LOFAR image and partially to an intrinsic larger extent of the source at low frequencies, especially of the southern lobe.

The total flux density of the outer lobes at 145 MHz is 285 mJy (obtained as the difference between the total flux density of the source and the peak flux density of the central

component) and their average surface brightness is equal to 4.7 mJy arcmin^{-2}. We note that the outer lobes represent only ~6% of the entire radio emission of the source at 145 MHz.

Due to the lower angular resolution of the LOFAR map, the S-shape morphology that is clearly visible in the map at 1400 MHz presented by Shulevski et al. (2012; see Fig. 1) is here less pronounced. However, we can still recognize two enhancements in surface brightness along the eastern edge of the northern outer lobe and the western edge of the southern outer lobe close to the core.

In the SRT image at 6600 MHz, the northern outer lobe is clearly detected too, although not for its entire extension (see Fig. 2, bottom panel). Unfortunately, the low resolution of the map does not allow us to study the lobe sub-structures. The southern outer lobe is completely blended with the unrelated source in south-east direction as well with the central CSS source itself, preventing us from any further analysis.

4.2. Spectral properties

4.2.1. Northern outer lobe

To measure the spectral index of the northern lobe we have convolved the new LOFAR image and the WSRT image produced by Shulevski et al. (2012) to the resolution of the SRT map at 6600 MHz equal to 2.9 arcmin. Because the instruments used in this work differ a lot from each other it is worth addressing the problem of the missing flux density. As this is not an issue for the single dish observations, it may become significant when using interferometers. The total flux density of an extended structure in a radio map can indeed be underestimated if the uv-plane does not provide enough uv-coverage at short spacings. An interferometer is sensitive to all the signal which is coming from structures in the sky with sizes $<0.6\lambda/D_{\min}$, where $D_{\min}$ is its shortest baseline (Tamhane et al. 2015). The angular size of the northern lobe is ~4.5 arcmin × 2.5 arcmin. The minimum observed baselines in the different observations are $D_{\min,145\,\mathrm{MHz}} \simeq 40\,\mathrm{m}$, $D_{\min,350\,\mathrm{MHz}} \simeq 85\,\mathrm{m}$ and $D_{\min,1400\,\mathrm{MHz}} \simeq 30\,\mathrm{m}$ giving a largest angular scale (θ, LAS) equal to $\theta_{145\,\mathrm{MHz}} \simeq 1.7\,\mathrm{deg}$, $\theta_{350\,\mathrm{MHz}} \simeq 21\,\mathrm{arcmin}$ and $\theta_{1400\,\mathrm{MHz}} \simeq 14\,\mathrm{arcmin}$ respectively. We, therefore, should be able to safely detect all the extended emission at all frequencies and making consistent comparisons between single-dish and interferometric data.

We have extracted the flux density from one region drawn in correspondence of the northern lobe (region_north) as shown in Fig. 3 (top panel). The measured values are reported in Table 4. The errors on the flux densities are computed by combining in quadrature the flux scale error and the image noise as shown in Klein et al. (2003). The spectral index analysis in this region reveals a spectrum with very little curvature over the entire frequency range 145–6600 MHz with $\alpha_{1400}^{145} = 0.48 \pm 0.11$ and $\alpha_{6600}^{1400} = 0.69 \pm 0.20$. The spectral curvature (SPC), defined as $\alpha_{6600}^{1400} - \alpha_{1400}^{145}$ (Murgia et al. 2011), is equal to SPC $\simeq 0.2 \pm 0.2$, well below the typical value of SPC > 0.5 expected for ageing plasma. Errors on the spectral indices are computed using the following expression:

$$\alpha_{\mathrm{err}} = \frac{1}{\ln \frac{\nu_1}{\nu_2}} \sqrt{\left(\frac{S_{1,\mathrm{err}}}{S_1}\right)^2 + \left(\frac{S_{2,\mathrm{err}}}{S_2}\right)^2} \qquad (1)$$

where S_1 and S_2 are the flux densities at frequencies ν_1 and ν_2 and $S_{1,\mathrm{err}}$ and $S_{2,\mathrm{err}}$ are the respective errors.
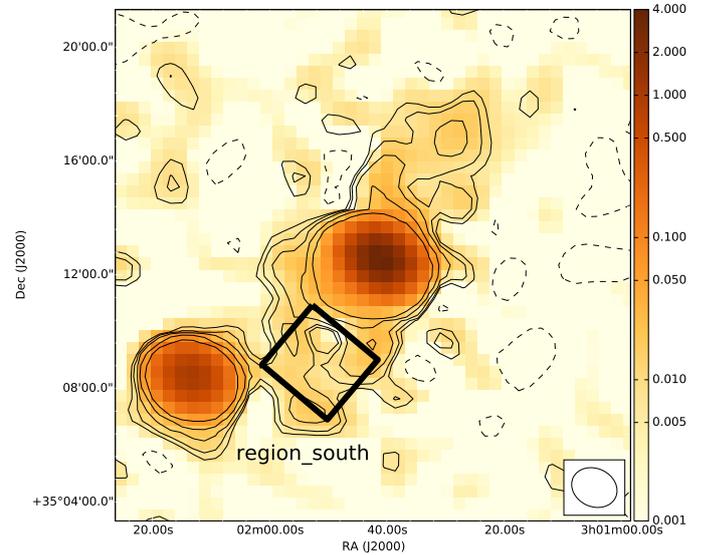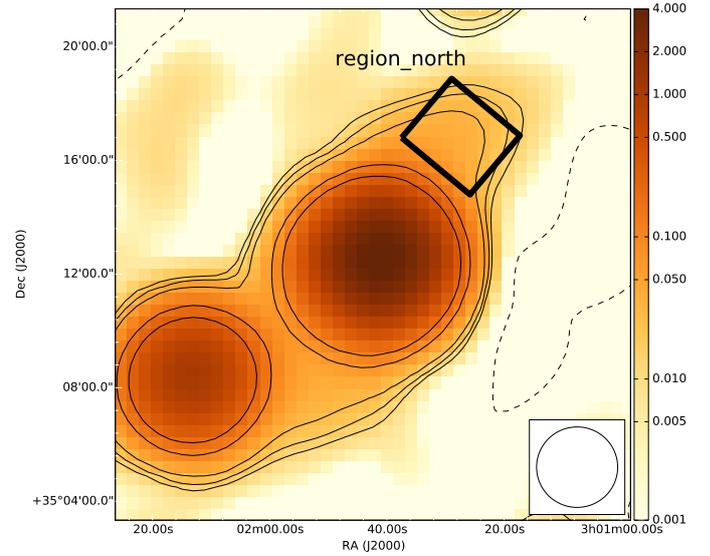
Fig. 3. *Top panel*: LOFAR image at 145 MHz convolved to 2.9-arcmin resolution. Contours represent $-2, 2, 3, 5, 10, 20 \times \sigma$ (5 mJy beam^{-1}). *Bottom panel*: LOFAR image at 145 MHz and 80 arcsec × 98 arcsec resolution. Contours represent $-2, 2, 3, 5, 10, 20 \times \sigma$ (3 mJy beam^{-1}). The black regions represent the boxes used to extract the flux density in the northern lobe and southern lobe respectively. The colour scale is set in Jy beam^{-1}.

4.2.2. Southern outer lobe

A measure of the flux density of the southern lobe is only possible at 145 MHz and at 1400 MHz. To make this measurement we have convolved the WSRT image to the resolution of the LOFAR image of 80 arcsec × 98 arcsec. We have extracted the flux density from one region drawn in correspondence of the southern lobe as shown in Fig. 3 (bottom panel, region_south). The measured values are reported in Table 4. The spectral index is $\alpha_{1400}^{145} = 0.73 \pm 0.07$ and is reported in Table 5.

4.3. Energetics and age of the outer radio lobes

Using the observed properties of the outer lobe radio emission at different frequencies we can, to first order, evaluate some physical parameters of the radio plasma.

Table 4. Flux densities of the northern lobe extracted from the radio images at 2.9-arcmin resolution and of the southern lobe extracted from the radio images at 80 arcsec × 98 arcsec resolution.

Frequency (MHz)	Flux density region_north (mJy)	Flux density region_south (mJy)
145	26.4 ± 5.6	68.1 ± 8.0
1400	9.0 ± 1.5	13.4 ± 1.3
6600	3.1 ± 0.9	–

Notes. Region_north and region_south are shown in Fig. 3.

Table 5. Spectral indices computed for the northern lobe using region_north and for the southern lobe using region_south (see Table 4 and Fig. 3).

Spectral index	region_north	region_south
α_{1400}^{145}	0.48 ± 0.11	0.73 ± 0.07
α_{6600}^{1400}	0.69 ± 0.20	–
α_{6600}^{145}	0.56 ± 0.09	–

Assuming equipartition conditions between particles and magnetic field, we have computed an average magnetic field value over the entire extension of the two outer lobes equal to $B_{eq} = 1\,\mu G$ (Worrall & Birkinshaw 2006).

For this calculation we have assumed a power-law particle distribution of the form $N(\gamma) \propto \gamma^{-p}$ between a minimum and maximum Lorentz factor of $\gamma_{min} = 10$ and $\gamma_{max} = 10^6$, with p being the particle energy power index. We have calculated the volume of the source assuming a cylindrical geometry in the plane of the sky. The radius and height of the cylinder were measured using the 3σ contours as a reference in correspondence of the lobe maximum extension and are equal to $R = 2.5$ arcmin and $h = 12$ arcmin respectively. We have assumed that the particle energy content of the source to be equally distributed between heavy particles and electrons so that their ratio $k = 1$, and we have set $p = 2.0$ according to the observed low-frequency spectral shape where radiative energy losses are less significant. A value of $S_{1400} = 120$ mJy is used following Shulevski et al. (2012). Moreover, this computation assumes that the magnetic field is uniformly distributed in the lobe volume.

By using the magnetic field B_{eq} calculated in this way and a classical radiative ageing model (Kellermann 1964; Pacholczyk 1970) it is possible to get a first order estimate of the spectral age t_s of the particle population in the outer lobes. Indeed the age of the emitting particles remains encoded in the curvature of their radio spectrum. In particular, as the particles age with time, the spectrum gets progressively steeper at frequencies higher than a critical break frequency ν_b, due to preferential radiative cooling of high-energy particles. As already mentioned in Sect. 4.2, the spectrum of the northern lobe of the source B2 0258+35 only shows a little curvature over the entire observed frequency range 145–6600 MHz. This prevents us from properly modelling it to get a radiative age estimate. However, we can set a conservative upper limit to the source radiative age by assuming a lower limit to the spectral break equal to 1400 MHz, which corresponds to the highest frequency after which the spectrum starts showing a curvature. For this we use the following equation (Kardashev

1962; Murgia et al. 2011):

$$t_s = 1590 \frac{B_{eq}^{0.5}}{(B_{eq}^2 + B_{CMB}^2)\sqrt{\nu_b(1+z)}}, \qquad (2)$$

where t_s is in Myr, the magnetic field B_{eq} and inverse Compton equivalent field B_{CMB} are in μG and the break frequency ν_b is in GHz. We note that with such a low value of B_{eq}, the radiative cooling of the plasma is dominated by inverse Compton scattering of cosmic microwave background (CMB) photons. The CMB equivalent magnetic field equal to $B_{CMB} = 3.25 \times (1 + z)^2$ has a value of $B_{CMB} = 3.36\,\mu G$. In this way we get an upper limit on the lobe age equal to $\lesssim 110$ Myr. The upper limit value of the radiative age is expected to decrease if the magnetic field was here underestimated due, for example, to an excess of non-radiative particles with respect to electrons. This occurrence is considered typical of low power jets, where entrainment of massive particles from the external IGM is dominant due to turbulence (Croston 2008; Massaglia et al. 2016). We also note that by using an alternative derivation of the magnetic field by Beck & Krause (2005) the value lowers by almost a factor three, and this would cause the upper limit of the radiative age to increase. Finally, it should be kept in mind that some mechanisms, such as in situ particle re-acceleration, compression and mixing may affect this result as we discuss in Sect. 5.

4.4. The central compact source

The flux densities of the central compact source measured from our new images at different frequencies are listed in Table 6 and marked with an asterisk. The measurements have been performed on images having the same resolution at all frequencies (equal to 2.9 arcmin) by fitting a Gaussian function to the unresolved component. Flux densities at different frequencies collected from the literature using the NASA/IPAC Extragalactic Database are also listed in Table 6.

Thanks to the increased number of flux density measurements with respect to the work of Giroletti et al. (2005), especially at low frequency, we can now better recognize a spectral turnover between 100 and 200 MHz and a possible spectral break at frequencies higher than 5000 MHz (Fig. 4). We use the empirical relation between size and turnover frequency found by O'Dea & Baum (1997) to measure the expected turnover frequency. This correlation has been for long explained in terms of synchrotron-self absorption related to the small size of the radio source (e.g. Snellen et al. 2000, Fanti 2009). We note, however, that free-free absorption due to a dense ambient medium is also thought to play a role according to some observations (e.g. Callingham et al. 2015; Tingay et al. 2015) and simulations (Bicknell et al. 2018). Under these circustances the following computed numbers must be treated with care.

Using the correlation presented in Orienti & Dallacasa (2014) and a measured linear size for the CSS source equal to 3 kpc we compute a predicted turnover frequency equal to 320 MHz. However, if we deproject the linear size of the source using the inclination angle of 45 deg estimated by Giroletti et al. (2005) we get a size of 4.3 kpc and a corresponding turnover frequency equal to 260 MHz. Considered the large scatter present in the correlation (up to almost an order of magnitude), the result is consistent with the observations.

In order to better quantify the shape of the radio spectrum we have performed a spectral fitting using the software SYNAGE (Murgia et al. 1999). In particular, we have used the continuous injection spectral model $S_{CI}(\nu)$ (Kardashev 1962) modified by

Table 6. Flux densities of the central CSS source at different frequencies with respective references.

| Frequency (MHz)	Flux (Jy)	Reference
74	4.69 ± 0.51	Cohen et al. (2007)
80	8.00 ± 1.60	Slee (1995)
84	5.10 ± 0.30	Hurley-Walker et al. (2017)
115	4.90 ± 0.10	Hurley-Walker et al. (2017)
145[a]	4.82 ± 0.48	This work
150	4.50 ± 0.10	Hurley-Walker et al. (2017)
151	5.11 ± 0.17	Hales et al. (1993)
160	4.10 ± 0.60	Slee (1995)
178	5.00 ± 1.40	Pilkington & Scott (1965)
235[a]	4.06 ± 0.20	This work
327	3.91 ± 0.60	Rengelink et al. (1997)
350[a]	3.51 ± 0.18	This work
365	3.60 ± 0.04	Douglas et al. (1996)
612[a]	3.07 ± 0.15	This work
1400	1.70 ± 0.10	Brown et al. (2011)
1400	1.77 ± 0.26	White & Becker (1992)
1400	1.84 ± 0.27	Condon et al. (1998)
1400	1.80 ± 0.18	Shulevski et al. (2012)
1600	1.60 ± 0.24	Sanghera et al. (1995)
2380	1.40 ± 0.07	Dressel & Condon (1978)
4835	0.90 ± 0.10	Griffith et al. (1990)
4850	0.86 ± 0.13	Gregory & Condon (1991)
5000	0.92 ± 0.14	Sanghera et al. (1995)
6600[a]	0.73 ± 0.07	This work
8400	0.61 ± 0.05	Giroletti et al. (2005)
10700	0.58 ± 0.03	Kellermann & Pauliny-Toth (1973)
22500	0.250 ± 0.005	Giroletti et al. (2005)

Notes. [a]Observations presented in this work.

low-frequency synchrotron-self absorption (Pacholczyk 1970) presented in Murgia et al. (1999) and shown below:

$$S(\nu) \propto (\nu/\nu_1)^{\alpha+\beta}(1 - e^{-(\nu/\nu_1)^{-(\alpha+\beta)}}) \cdot S_{CI}(\nu), \qquad (3)$$

where ν_1 is the frequency at which the optical depth is equal to 1, α is the spectral index in the transparent frequency range and β is the coefficient for an homogeneous synchrotron self-absorbed source and is fixed to 2.5. For the fitting the flux density errors at all frequencies have been set to a systematic value equal to 10%. We fix the injection index α_{inj} to a classical value of 0.5 and we find a break frequency equal to $\nu_b = 21800 \pm 8200$ MHz and a synchrotron self-absorption frequency equal to $\nu_{SSA} = 79 \pm 10$ MHz. For comparison, we have also fitted the model setting the injection index α_{inj} as a free parameter. In this case we find a break frequency equal to $\nu_b = 6400 \pm 3700$ MHz and a synchrotron self-absorption frequency equal to $\nu_{SSA} = 65 \pm 24$ MHz. We have used the statistical F-test to select the best model and find that the model with free α_{inj} does not improve the fitting with a confidence level of 95%. Therefore, we consider the model with fixed α_{inj} as the best fit model and we will refer to its results in the following discussion. The integrated spectrum of the central CSS source and the results from the best model fitting are presented in Fig. 4. Our new measurements, indicated as red squares in the figure, nicely follow the literature points, which are shown as black open circles.

The resulting $\nu_b = 21800 \pm 8200$ MHz is higher than the value estimated by Giroletti et al. (2005) equal to 4600 MHz. Assuming a magnetic field equal to $B_{eq} = 90 \mu G$ (Giroletti et al. 2005) and using Eq. (2), we get an estimate of the particle radiative age
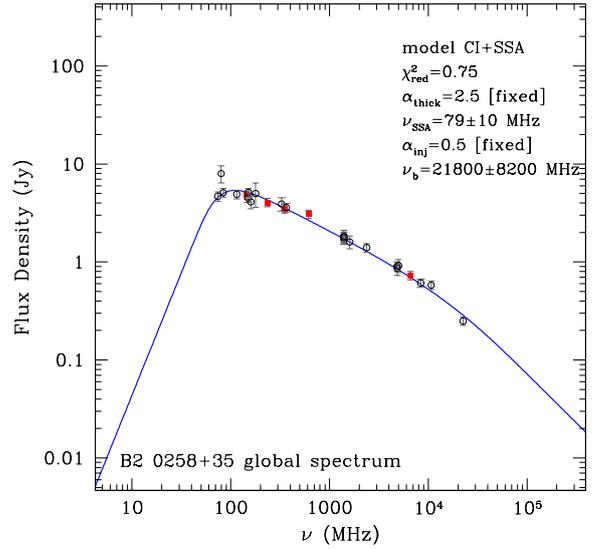
Fig. 4. Integrated radio spectrum of the central CSS source and best fit model. Red squares represent the flux density measurements presented in this paper, while black open circles are taken from literature. The entire list of flux densities used in the plot with respective errors and references is presented in Table 6.

equal to 0.4 Myr. Despite the updated age for the CSS source is lower than the previous estimate by Giroletti et al. (2005) (0.9 Myr), it remains high when compared with sources of similar size studied in the literature (Murgia 2003). This may support a scenario where the expansion of the lobes is impeded by a dense interstellar medium as suggested by Giroletti et al. (2005) and further explored by the study of the HI gas by Murthy et al. (in prep.).

5. Discussion

Due to their very low surface brightness and amorphous morphology, the outer lobes of B2 0258+35 have been previously suggested to be old remnants of a past episode of AGN activity. The increase in frequency coverage presented in this work allows us to make a step forward in the understanding of the nature of these structures and in the overall radio galaxy evolution as we describe below.

5.1. Source characteristics

Our new LOFAR observations at 145 MHz show that the outer lobes of B2 0258+35 have a total linear extension of 265 kpc and a relaxed shape with low surface brightness (4.7 mJy arcmin^{-2} at 145 MHz) in agreement with the previous study at 1400 MHz (Shulevski et al. 2012). The surface brightness values are consistent with other observations of remnant radio lobes (e.g. 4 mJy arcmin^{-2}, Brienza et al. 2016; 2.5–6 mJy arcmin^{-2}, Saripalli et al. 2012), a few giant radio galaxy lobes (e.g. 1 mJy arcmin^{-2}, Saripalli et al. 2012; 10 mJy arcmin^{-2}, Subrahmanyan et al. 2006) and the radio galaxy NGC 3998 (5 mJy arcmin^{-2}, Frank et al. 2016). The outer lobes are so faint that they only represent ~6% of the entire source luminosity. This extreme contrast in surface brightness between the inner and outer structure represents, to date, a quite rare case among the radio galaxy population as further discussed is Sect. 5.3. Because the host galaxy is located in a low density environment, the plasma of the outer lobes may have suffered a

severe adiabatic expansion and a consequent surface brightness decrease. However, if this is the case, we would expect the outer lobes to dissipate very quickly in the ambient medium. High-sensitivity X-ray observations would be needed to probe the pressure balance between the lobes and the surrounding IGM. At the same time, if the inner jets have strong interactions with the surrounding ISM, the radio luminosity may be boosted due to compression of the magnetic field and the increased particle density (Morganti et al. 2011; Tadhunter et al. 2011; Giroletti et al. 2005).

Other features that are interesting to discuss and may provide hints for the interpretation of the source are the broad enhancements in surface brightness present at the edges of the outer lobes. One possible explanation is that this S-shape structure represents an active channel of plasma connecting the inner and outer lobes. Alternatively, it could represent remnant large-scale jets from the previous cycle of activity. The reason for the bent geometry of these features remains unclear though. One possibility is that the jets are bent as a result of the strong interaction with the dense nuclear ISM. Otherwise the jets may have been subject to precession. Precession of radio jets have been observed in radio galaxies (e.g. Falceta-Gonçalves et al. 2010; Gong et al. 2011; Nawaz et al. 2016). Models show that on such large spatial scales precession can only happen on timescales larger than 1–10 Myr (e.g. Nixon & King 2013), which would be compatible with the timescales we have estimated for the radio galaxy B2 0258+35. The origin of the phenomenon is typically connected to gas misalignments in the accretion disk, which are often a consequence of a merger event, although it is still not completely clear how the timescales of these instabilities and the precession of kiloparsec-scale jets relate (e.g. Lu & Zhou 2005). Whether the source B2 0258+35 has actually experienced accretion instabilities is difficult to assess. Shulevski et al. (2012) investigate extensively different scenarios for the black hole gas supply and triggering based on the results of the gas kinematics of Struve et al. (2010), Emonts (2006) and Prandoni et al. (2007). From that, they exclude a direct link between the merger history of the source and the duty cycle of the radio activity. They suggest instead that the black hole is accreting gas that is cooling from the galaxy's hot corona via Bondi accretion (Bondi 1952; Hardcastle et al. 2007). In this case, chaotic accretion of cold gas clouds condensed from the hot atmosphere may also take place as suggested by a few authors (e.g. Soker et al. 2009; Pizzolato & Soker 2010; Gaspari et al. 2013, 2017). This may be responsible for the accretion instabilities required by precession models, as well as they could justify the jet time discontinuity. Moreover, we cannot exclude that some interactions with the small gas-rich satellites that surround the host galaxy may have disturbed the accretion process and influenced the AGN duty cycle.

Beside the morphology, another interesting property of the outer lobes is the spectral shape. We find that the radio spectrum of neither the northern lobe nor the southern lobe is ultra-steep ($\alpha > 1.2$), as expected for an old ageing plasma. Moreover, despite the wide frequency coverage available for the northern lobe (145–6600 MHz), no significant spectral curvature is identified (see Sect. 4.2). Based on the spectral slope and using a simple radiative model, we have derived a first order upper limit to the plasma age in the northern lobe equal to <110 Myr (see Sect. 4.3). We stress that if mechanisms such as particle re-acceleration, mixing or compression are in action, this age estimate does not hold anymore as it is further discussed in Sect. 5.2). By treating the lobes as buoyant bubbles expanding in the intergalactic medium (IGM) with a rising speed of

~613 km s^{-1}, Shulevski et al. (2012) have estimated that the time elapsed since the jet activity has ceased is equal to $\gtrsim$80 Myr (the lower limit is introduced to take into account a possible inclination angle). This value, however, can also be interpreted as an upper limit to the entire age of the outer lobes if we consider that the outer lobes must have expanded to the current size already during the jet activity. In this case the lobes, pushed by the jets advance, should have expanded faster than what assumed by the buoyancy scenario. With this assumption the dynamical age of the outer lobes is consistent with the radiative age upper limit computed in this work.

5.2. Source evolutionary scenarios and duty cycle

The characteristics of the source B2 0258+35 are exceptional and a unique interpretation of the source's evolution remains difficult to assess. Here we propose three evolutionary scenarios to explain the spectral and morphological properties discussed above.

1. The radio AGN has never switched off. Instead, the large-scale jets have been temporarily disrupted and smothered by e.g. the interaction of the particle flows with a dense medium as suggested by Baum et al. (1990). In this case the two enhancements in surface brightness visible at the edges of the outer lobes could represent two uncollimated jets that connect the outer and inner structure. Under this circumstance the outer lobes would still be fuelled with fresh particles, even if at a low rate, and this would explain the small spectral curvature. This scenario may be consistent with the idea of the inner lobes currently being confined or impeded by a dense interstellar medium as suggested by Giroletti et al. (2005) and Murty et al. (in prep.).

2. The radio AGN has actually stopped and restarted after a short amount of time. The outer lobes could be currently disconnected from the inner jets and therefore not replenished with fresh particles. However, if the time elapsed since the AGN switch off is not too long, it is possible that the spectral steepening produced by particle ageing in the outer lobes is still not prominent in the considered spectral range (145–6600 MHz). The low level of magnetic field observed would also contribute to make the spectral evolution slow. In this case the two enhancements in surface brightness discussed above could be interpreted as the channels of the previously active jets that have recently stopped to be fuelled. Assuming this scenario, we can use the timescales presented in Sect. 4.3 to place an upper limit to the time elapsed between the two phases of jet activity equal to $\lesssim$100 Myr, by combining the radiative age estimate for the outer lobes (<110 Myr, see Sect. 4.3) with the CSS radiative age equal to 0.4 Myr (see Sect. 4.4). This is in agreement with the initial estimate by Shulevski et al. (2012). Higher frequency observations would be needed to set tighter constraints on the radiative age of the outer lobes and therefore on the duty cycle. Unfortunately such high sensitivity observations on such large spatial scales are difficult to obtain.

3. The outer lobes are remnants of a previous AGN activity and are detached from the current nuclear activity but they do not show an important spectral curvature because of mechanisms such as in situ particle reacceleration, adiabatic compression and particle mixing. All these mechanisms represent valid alternatives to explain the small spectral curvature as they influence the spectral evolution. We stress that, in this case, the computation of the radiative age presented above is not valid. In particular, particle re-acceleration tend to

increase the energy of high energy particles causing a "flattening" of the high-frequency tail of the observed radio spectrum (Alexander 1987). This phenomenon may be caused by shocks, like backflows in lobes of active radio galaxies, or stochastic processes, like plasma turbulence. In this occurrences we would also expect significant mixing of particles of different ages within the outer lobes and this would contribute to erase the spectral curvature (Turner et al. 2018). By increasing the kinetic energy of the particle population and thus shifting the break frequency to higher frequencies, adiabatic compression may also have a role in contaminating the radiative age estimate (Scheuer & Williams 1968; Alexander 1987). In this case, Alexander (1987) suggests that some brightness enhancement should be observed together with some polarized emission produced by the compressed magnetic plasma (Laing 1980).

For the source B2 0258+35, re-acceleration and particle mixing may be compatible with the presence of turbulence created as a consequence of the shock evolution, between the low-power jets and the ambient medium (Croston 2008; Massaglia et al. 2016). Adiabatic compression also represents an interesting possibility. As mentioned in Sect. 4.1, the outer lobes show at both 145 and 1400 MHz two surface brightness enhancements at the edge of each lobe in specular position with respect to the core that could fit the expected features for adiabatic compression. Polarization information will be used to test this hypothesis (Adebahr et al., in prep.).

Discriminating among the above-mentioned scenarios and providing tight constrain on the duty cycle of B2 0258+35 is difficult. However, our results seem to suggest that in no case the outer lobes are compatible with very old remnants as the morphology alone would suggest and as it was previously proposed. Indeed, all of the mechanisms considered above to explain the small spectral curvature become irrelevant after some time after the large scale jets have switched off. For example Eilek (2014) estimates that, for the case of Centaurus A, the decay time of the turbulence is of the order of few tens of Myr after which the lobes should quickly fade away. By assuming comparable values of turbulence decay for B2 0258+35, it follows that, either the lobes are still fuelled by the nuclear activity or the switch off must have happened only few tens of Myr ago, suggesting a quiescent phase shorter than a few tens of Myr, contrary to previous expectations.

5.3. Comparison with other radio galaxies

As already mentioned above, the properties of B2 0258+35 are peculiar among radio galaxies. However, we have recognized a small number of objects that show some comparable characteristics as described below.

A few sources, for example, show some inner and outer lobes with a very high surface brightness contrast as observed in B2 0258+35 and for this reason are claimed to be restarted radio galaxies. Among these there are the radio galaxy associated with NGC 3998 ($\sim$20 kpc, Frank et al. 2016), the source 4C 29.30 ($\sim$600 kpc, Jamrozy et al. 2007), the misaligned DDRG 3C293 (190 kpc, Joshi et al. 2011; Machalski et al. 2016), the source Mrk 6 (7.5 kpc, Kharb et al. 2006) and the well-known radio galaxy Centaurus A ($\sim$200 kpc, McKinley et al. 2018; Morganti et al. 1999). Moreover, we note some similarity with the famous radio galaxies M87 (e.g. Owen et al. 2000) and 3C317 (Zhao et al. 1993; Venturi et al. 2004). Particularly interesting is the halo of the source M87, which seems to be made of a superposition of many plasma bubbles of different ages and does

not show any significant spectral curvature in its spectrum, with no clear relation between the spectral index and the brightness distribution at low frequencies (de Gasperin et al. 2012). It is interesting to note that some of these sources, that is, NGC 3998, Mrk 6 and Centaurus A show a similar S-shape morphology to B2 0258+35. The origin of this shape has been suggested to be related to a change of angular momentum in the accreting gas or to an episodically powered precessing jet (Frank et al. 2016; Kharb et al. 2006).

From a spectral point of view we find a striking resemblance between B2 0258+35 and Centaurus A. Indeed, the radio spectrum of the northern outer lobe of Centaurus A is not ultra-steep up to 90 000 MHz (Hardcastle et al. 2009; Alvarez et al. 2000) and its age is estimated to range between few tens of Myr (using radiative models, Hardcastle et al. 2009) and >100 Myr (using dynamical models, Saxton et al. 2001). While, in situ particle reacceleration is claimed to be a key component for preventing the spectrum from steepening at high frequency, the discovery of an intermediate-scale northern middle lobe (Morganti et al. 1999; McKinley et al. 2013, 2018) suggests the presence of an "open channel" of fresh particles between the inner and the outer lobe.

While all the afore-mentioned radio galaxies show signs of recurrent jet activity, the origin and timescales of this intermittence are still unclear. The sources 3C317 and M87 are located at the centre of massive clusters of galaxies so they are most likely going through a short, self-regulating AGN feedback cycle with the surrounding hot medium.

All the other sources presented above, including B2 0258+35, are located instead in low density environments. Therefore, their jet activity is expected to be triggered less frequently. It is worth noting though, that they all show signatures of past merger events and a large reservoir of gas in different phases (e.g. HI, CO).

Mergers are often claimed to be responsible for the triggering of the AGN in galaxies. However, the timescales of the radio activity are usually found to be much shorter (10^6-10^7 yr) than those computed for the merger events (10^8-10^9 yr), making the connection between the two phenomena weak (e.g. Emonts 2006; Struve et al. 2010; Maccagni et al. 2014). More compatible timescales (10^5-10^7 yr) come from multiple galaxy encounters that preceed the merger event and can increase the gas kinematical instabilities in the host galaxy, as suggested for explaining the origin of DDRGs (Schoenmakers et al. 2000).

Alternatives that do not require any external contribution are instabilities in the accretion disk, for instance caused by the radiation pressure induced warping (Pringle 1997; Czerny et al. 2009), or chaotic accretion of cold gas clouds (Soker et al. 2009; Gaspari et al. 2013, 2017). This last scenario looks particularly promising especially in gas rich galaxies like those analysed here. Indeed, local instabilities occurring in the observed gas structures (such as the HI disk in B2 0258+35) may cause an infall of clouds towards the galaxy centre, which may trigger the AGN frequently and intermittently (see Soker et al. 2009; Gaspari et al. 2013, 2017).

6. Conclusions and future work

In this paper we have presented new multi-frequency observations of the source B2 0258+35 aimed at investigating the properties of the outer lobes initially identified by Shulevski et al. (2012) at 1400 MHz. The lobes are further detected at 145 MHz with LOFAR and at 6600 MHz with SRT. The main findings are summarized below:

(i) New observations with LOFAR at 145 MHz confirm the size (~265 kpc), relaxed shape and low surface brightness of the outer lobes previously observed at 1400 MHz by Shulevski et al. (2012). The emission from the outer lobes only represent ~6% of the entire source luminosity at 145 MHz. The extreme luminosity contrast between the inner and outer structure might be explained, on one hand, by strong adiabatic expansion of the plasma of the outer lobes in the ambient medium and, on the other hand, by a luminosity boost of the inner lobes due to compression of the magnetic field and the increased density of particles.

(ii) The S-shape morphology observed in the map at 1400 MHz is visible in the LOFAR map too, although much less pronounced due to the lower angular resolution. This structure may be interpreted as due to low power jets that connect the inner and outer lobes or to jet remnants from the previous cycle of activity. The S-shape may have originated from the jets bending due to a dense ISM or from precession.

(iii) The combination of the new LOFAR and SRT observations with the data at 1400 MHz shows that the integrated spectrum of the outer northern lobe is not ultra steep and does not present a significant spectral curvature (SPC ∼ 0.2 ± 0.2) with spectral indices equal to $\alpha^{145}_{1400} = 0.48 \pm 0.11$ and $\alpha^{1400}_{6600} = 0.69 \pm 0.20$. The spectral index in the outer southern lobe in the range 145–1400 MHz is $\alpha^{145}_{1400} = 0.73 \pm 0.07$.

(iv) By assuming a simple radiative model to describe the integrated spectrum of the outer northern lobe we have computed a first order upper limit to the radiative age equal to ≲110 Myr. This value is compatible with the dynamical age computed by Shulevski et al. (2012) and provides an estimate of the jet quiescent time between the two subsequent phases of activity equal to ≲100 Myr. We stress that this value should be treated with care as it neglects mechanisms such as situ particle reacceleration, mixing and/or adiabatic compression that may alter the spectral shape.

(v) Possible evolutionary scenarios to explain the source morphology and spectral properties of the outer lobes are the following: (1) the AGN has never switched off but the large-scale radio jets have only been temporarily disrupted. The outer lobes are still fuelled by fresh particles from the nucleus at a very low rate; (2) the active nucleus has switched off and on again after a short time so that the plasma in the outer lobes is still not aged; (3) the outer lobes are remnants of a previous AGN activity but in situ particle reacceleration, mixing and/or adiabatic compression prevent their spectrum from further steepening.

(vi) As all the mechanisms mentioned above stop to be relevant on timescales longer than a few tens of Myr, it follows that the outer lobes are not very old remnants as the morphology alone would suggest and as it was previously claimed. Instead, we propose that either the outer lobes are still fuelled by the nuclear activity or the switch off must have happened only few tens of Myr ago, suggesting a jet quiescent phase shorter than a few tens of Myr.

(vii) Future searches of restarted radio galaxies should bear in mind that not all low-surface brightness lobes and halos with amorphous shape that are found around compact, bright jets are necessarily ultra-steep spectrum remnants of past AGN activity. This is especially true for low power radio galaxies.
The morphological and the spectral characteristics of the source B2 0258+35 are quite exceptional and only a small number of other radio galaxies show some resemblance. Analysis of its polarization properties will be used to further investigate the nature of the outer lobes and the source evolution (Adebahr et al. in prep.).

To date, it is not clear whether these sources are intrinsically rare or whether they have just been missed by the old-generation instruments, due to their lack of sensitivity, especially at low frequency. LOFAR is the perfect instrument to clarify this as it provides at the same time high spatial resolution (20 arcsec up to 6 arcsec) and high sensitivity (with typical noise values up to 0.1 mJy beam^{-1} in 8 h observations) at 145 MHz. By using LoTSS we are starting a systematic search for low surface brightness, extended emission around a sample of well-known compact radio galaxies (< few kpc) that are located in the survey area. Low frequency data will be able to probe even the most aged particle population. With this we will get a better statistics of the presence of such extended structures around compact radio galaxies and we will be able to investigate their properties and nature in a statistical way.

References

Alexander, P. 1987, MNRAS, 225, 27
Alvarez, H., Aparici, J., May, J., & Reich, P. 2000, A&A, 355, 863
Baum, S. A., O'Dea, C. P., Murphy, D. W., & de Bruyn, A. G. 1990, A&A, 232, 19
Beck, R., & Krause, M. 2005, Astron. Nachr., 326, 414
Best, P. N., Kauffmann, G., Heckman, T. M., et al. 2005, MNRAS, 362, 25
Bhatnagar, S., Cornwell, T. J., Golap, K., & Uson, J. M. 2008, A&A, 487, 419
Bicknell, G. V., Mukherjee, D., Wagner, A. Y., Sutherland, R. S., & Nesvadba, N. P. H. 2018, MNRAS, 475, 3493
Bolli, P., Orlati, A., Stringhetti, L., et al. 2015, J. Astron. Instrum., 4, 1550008
Bondi, H. 1952, MNRAS, 112, 195
Brienza, M., Godfrey, L., Morganti, R., et al. 2016, A&A, 585, A29
Brienza, M., Godfrey, L., Morganti, R., et al. 2017, A&A, 606, A98
Brown, M. J. I., Jannuzi, B. T., Floyd, D. J. E., & Mould, J. R. 2011, ApJ, 731, L41
Callingham, J. R., Gaensler, B. M., Ekers, R. D., et al. 2015, ApJ, 809, 168
Cohen, A. S., Lane, W. M., Cotton, W. D., et al. 2007, AJ, 134, 1245
Condon, J. J., Cotton, W. D., Greisen, E. W., et al. 1998, AJ, 115, 1693
Cornwell, T. J., & Perley, R. A. 1992, A&A, 261, 353
Croston, J. H. 2008, in Extragalactic Jets: Theory and Observation from Radio to Gamma Ray, eds. T. A. Rector, & D. S. De Young, ASP Conf. Ser., 386, 335
Czerny, B., Siemiginowska, A., Janiuk, A., Nikiel-Wroczyński, B., & Stawarz, Ł. 2009, ApJ, 698, 840
de Gasperin, F., Orrú, E., Murgia, M., et al. 2012, A&A, 547, A56
Di Matteo, T., Springel, V., & Hernquist, L. 2005, Nature, 433, 604
Douglas, J. N., Bash, F. N., Bozyan, F. A., Torrence, G. W., & Wolfe, C. 1996, AJ, 111, 1945

Dressel, L. L., & Condon, J. J. 1978, ApJS, 36, 53
Eilek, J. A. 2014, New J. Phys., 16, 045001
Emonts, B. H., 2006, PhD Thesis, University of Groningen, The Netherlands
Emonts, B. H. C., Morganti, R., Struve, C., et al. 2010, MNRAS, 406, 987
Fabian, A. C. 2012, ARA&A, 50, 455
Falceta-Gonçalves, D., Caproni, A., Abraham, Z., Teixeira, D. M., & de Gouveia Dal Pino, E. M. 2010, ApJ, 713, L74
Fanti, C. 2009, Astron. Nachr., 330, 120
Frank, B. S., Morganti, R., Oosterloo, T., Nyland, K., & Serra, P. 2016, A&A, 592, A94
Gaspari, M., Brighenti, F., & Temi, P. 2012, MNRAS, 424, 190
Gaspari, M., Ruszkowski, M., & Oh, S. P. 2013, MNRAS, 432, 3401
Gaspari, M., Temi, P., & Brighenti, F. 2017, MNRAS, 466, 677
Giovannini, G., Cotton, W. D., Feretti, L., Lara, L., & Venturi, T. 2001, ApJ, 552, 508
Giroletti, M., Giovannini, G., & Taylor, G. B. 2005, A&A, 441, 89
Godfrey, L. E. H., Morganti, R., & Brienza, M. 2017, MNRAS, 471, 891
Gong, B. P., Li, Y. P., & Zhang, H. C. 2011, ApJ, 734, L32
Govoni, F., Murgia, M., Vacca, V., et al. 2017, A&A, 603, A122
Gregory, P. C., & Condon, J. J. 1991, ApJS, 75, 1011
Griffith, M., Langston, G., Heflin, M., et al. 1990, ApJS, 74, 129
Hales, S. E. G., Baldwin, J. E., & Warner, P. J. 1993, MNRAS, 263, 25
Hardcastle, M. J., Evans, D. A., & Croston, J. H. 2007, MNRAS, 376, 1849
Hardcastle, M. J., Cheung, C. C., Feain, I. J., & Stawarz, Ł. 2009, MNRAS, 393, 1041
Heald, G., McKean, J., Pizzo, R., et al. 2010, in ISKAF2010 Science Meeting, 57
Ho, L. C., Filippenko, A. V., & Sargent, W. L. W. 1997, ApJS, 112, 315
Hurley-Walker, N., Johnston-Hollitt, M., Ekers, R., et al. 2015, MNRAS, 447, 2468
Hurley-Walker, N., Callingham, J. R., Hancock, P. J., et al. 2017, MNRAS, 464, 1146
Intema, H. T. 2014, Astron. Soc. India Conf. Ser., 13
Intema, H. T., Jagannathan, P., Mooley, K. P., & Frail, D. A. 2017, A&A, 598, A78
Jamrozy, M., Konar, C., Saikia, D. J., et al. 2007, MNRAS, 378, 581
Jamrozy, M., Saikia, D. J., & Konar, C. 2009, MNRAS, 399, L141
Joshi, S. A., Nandi, S., Saikia, D. J., Ishwara-Chandra, C. H., & Konar, C. 2011, MNRAS, 414, 1397
Kaiser, C. R., Schoenmakers, A. P., & Röttgering, H. J. A. 2000, MNRAS, 315, 381
Kardashev, N. S. 1962, Sov. Astron., 6, 317
Kellermann, K. I. 1964, ApJ, 140, 969
Kellermann, K. I., & Pauliny-Toth, I. I. K. 1973, AJ, 78, 828
Kharb, P., O'Dea, C. P., Baum, S. A., Colbert, E. J. M., & Xu, C. 2006, ApJ, 652, 177
Klein, U., Mack, K.-H., Gregorini, L., & Vigotti, M. 2003, A&A, 406, 579
Konar, C., & Hardcastle, M. J. 2013, MNRAS, 436, 1595
Konar, C., Hardcastle, M. J., Jamrozy, M., & Croston, J. H. 2013, MNRAS, 430, 2137
Kuźmicz, A., Jamrozy, M., Kozieł-Wierzbowska, D., & Weżgowiec, M. 2017, MNRAS, 471, 3806
Laing, R. A. 1980, MNRAS, 193, 439
Loi, F., Murgia, M., Govoni, F., et al. 2017, MNRAS, 472, 3605
Lu, J.-F., & Zhou, B.-Y. 2005, ApJ, 635, L17
Luo, W. F., Yang, J., Cui, L., Liu, X., & Shen, Z. Q. 2007, Chin. J. Astron. Astrophys., 7, 611
Maccagni, F. M., Morganti, R., Oosterloo, T. A., & Mahony, E. K. 2014, A&A, 571, A67
Machalski, J., Jamrozy, M., Stawarz, Ł., & Weżgowiec, M. 2016, A&A, 595, A46
Mahatma, V. H., Hardcastle, M. J., Williams, W. L., et al. 2018, MNRAS, 475, 4557
Mahony, E. K., Morganti, R., Prandoni, I., et al. 2016, MNRAS, 463, 2997
Massaglia, S., Bodo, G., Rossi, P., Capetti, S., & Mignone, A. 2016, A&A, 596, A12
McKinley, B., Briggs, F., Gaensler, B. M., et al. 2013, MNRAS, 436, 1286
McKinley, B., Tingay, S. J., Carretti, E., et al. 2018, MNRAS, 474, 4056
McMullin, J. P., Waters, B., Schiebel, D., Young, W., & Golap, K. 2007, in Astronomical Data Analysis Software and Systems XVI, eds. R. A. Shaw, F. Hill, & D. J. Bell, ASP Conf. Ser., 376, 127
McNamara, B. R., & Nulsen, P. E. J. 2007, ARA&A, 45, 117
Melis, A., Concu, R., Trois, A., et al. 2018, J. Astron. Instrum., 7, 1850004
Morganti, R. 2017, Nat. Astron., 1, 596

Morganti, R., Killeen, N. E. B., Ekers, R. D., & Oosterloo, T. A. 1999, MNRAS, 307, 750
Morganti, R., Holt, J., Tadhunter, C., et al. 2011, A&A, 535, A97
Murgia, M. 2003, PASA, 20, 19
Murgia, M., Fanti, C., Fanti, R., et al. 1999, A&A, 345, 769
Murgia, M., Parma, P., Mack, K.-H., et al. 2011, A&A, 526, A148
Murgia, M., Govoni, F., Carretti, E., et al. 2016, MNRAS, 461, 3516
Nawaz, M. A., Bicknell, G. V., Wagner, A. Y., Sutherland, R. S., & McNamara, B. R. 2016, MNRAS, 458, 802
Nixon, C., & King, A. 2013, ApJ, 765, L7
Noordermeer, E., van der Hulst, J. M., Sancisi, R., Swaters, R. A., & van Albada, T. S. 2005, A&A, 442, 137
O'Dea, C. P., & Baum, S. A. 1997, AJ, 113, 148
Orienti, M., & Dallacasa, D. 2008, A&A, 487, 885
Orienti, M., & Dallacasa, D. 2014, MNRAS, 438, 463
Orrù, E., van Velzen, S., Pizzo, R. F., et al. 2015, A&A, 584, A112
Owen, F. N., Eilek, J. A., & Kassim, N. E. 2000, ApJ, 543, 611
Pacholczyk, A. G. 1970, Radio Astrophysics. Nonthermal Processes in Galactic and Extragalactic Sources (San Francisco: Freeman)
Parma, P., Murgia, M., de Ruiter, H. R., et al. 2007, A&A, 470, 875
Perley, R. A., & Butler, B. J. 2013, ApJS, 204, 19
Pilkington, J. D. H., & Scott, J. F. 1965, MNRAS, 69, 183
Pizzolato, F., & Soker, N. 2010, MNRAS, 408, 961
Prandoni,, I., Laing, R. A.,, Parma, P., et al. 2007, in From Z-Machines to ALMA: (Sub)Millimeter Spectroscopy of Galaxies, eds. A. J. Baker, J. Glenn, A. I. Harris, J. G. Mangum, & M. S. Yun, ASP Conf. Ser., 375, 271
Prandoni, I., Murgia, M., Tarchi, A., et al. 2017, A&A, 608, A40
Pringle, J. E. 1997, MNRAS, 292, 136
Rengelink, R. B., Tang, Y., de Bruyn, A. G., et al. 1997, A&AS, 124, 259
Saikia, D. J., & Jamrozy, M. 2009, Bull. Astron. Soc. India, 37, 63
Sanghera, H. S., Saikia, D. J., Luedke, E., et al. 1995, A&A, 295, 629
Saripalli, L., Subrahmanyan, R., Thorat, K., et al. 2012, ApJS, 199, 27
Saxton, C. J., Sutherland, R. S., & Bicknell, G. V. 2001, ApJ, 563, 103
Scaife, A. M. M., & Heald, G. H. 2012, MNRAS, 423, L30
Schaye, J., Crain, R. A., Bower, R. G., et al. 2015, MNRAS, 446, 521
Scheuer, P. A. G., & Williams, P. J. S. 1968, ARA&A, 6, 321
Schoenmakers, A. P., de Bruyn, A. G., Röttgering, H. J. A., van der Laan, H., & Kaiser, C. R. 2000, MNRAS, 315, 371
Shabala, S. S., Ash, S., Alexander, P., & Riley, J. M. 2008, MNRAS, 388, 625
Shimwell, T. W., Röttgering, H. J. A., Best, P. N., et al. 2017, A&A, 598, A104
Shulevski, A., Morganti, R., Oosterloo, T., & Struve, C. 2012, A&A, 545, A91
Shulevski, A., Morganti, R., Harwood, J. J., et al. 2017, A&A, 600, A65
Sijacki, D., Vogelsberger, M., Genel, S., et al. 2015, MNRAS, 452, 575
Slee, O. B. 1995, Aust. J. Phys., 48, 143
Snellen, I. A. G., Schilizzi, R. T., Miley, G. K., et al. 2000, MNRAS, 319, 445
Soker, N., Sternberg, A., & Pizzolato, F. 2009, AIP Conf. Ser., 1201, 321
Struve, C., Oosterloo, T. A., Morganti, R., & Saripalli, L. 2010, A&A, 515, A67
Subrahmanyan, R., Hunstead, R. W., Cox, N. L. J., & McIntyre, V. 2006, ApJ, 636, 172
Swarup, G. 1991, in IAU Colloq. 131: Radio Interferometry. Theory, Techniques, and Applications, eds. T. J. Cornwell, & R. A. Perley, ASP Conf. Ser., 19, 376
Tadhunter, C., Holt, J., González Delgado, R., et al. 2011, MNRAS, 412, 960
Tamhane, P., Wadadekar, Y., Basu, A., et al. 2015, MNRAS, 453, 2438
Tasse, C., van der Tol, S., van Zwieten, J., van Diepen, G., & Bhatnagar, S. 2013, A&A, 553, A105
Tingay, S. J., Macquart, J.-P., Collier, J. D., et al. 2015, AJ, 149, 74
Turner, R. J., & Shabala, S. S. 2015, ApJ, 806, 59
Turner, R. J., Rogers, J. G., Shabala, S. S., & Krause, M. G. H. 2018, MNRAS, 473, 4179
Vacca, V., Murgia, M., & Loi, F. G. F. 2018, MNRAS, 479, 776
van Haarlem, M. P., Wise, M. W., Gunst, A. W., et al. 2013, A&A, 556, A2
van Weeren, R. J., Williams, W. L., Hardcastle, M. J., et al. 2016, ApJS, 223, 2
Venturi, T., Dallacasa, D., & Stefanachi, F. 2004, A&A, 422, 515
Wagner, A. Y., & Bicknell, G. V. 2011, ApJ, 728, 29
Wagner, A. Y., Bicknell, G. V., & Umemura, M. 2012, ApJ, 757, 136
Wegner, G., Haynes, M. P., & Giovanelli, R. 1993, AJ, 105, 1251
White, R. L., & Becker, R. H. 1992, ApJS, 79, 331
Williams, W. L., van Weeren, R. J., Röttgering, H. J. A., et al. 2016, MNRAS, 460, 2385
Worrall, D. M., & Birkinshaw, M. 2006, in Physics of Active Galactic Nuclei at all Scales, ed. D. Alloin (Berlin: Springer Verlag), Lect. Notes Phys., 693, 39
Wu, Q. 2009, ApJ, 701, L95
Zhao, J.-H., Sumi, D. M., Burns, J. O., & Duric, N. 1993, ApJ, 416, 51